J Ther Eng, Vol. 10, No. 1, pp. 21−35, January, 2024

Journal of Thermal Engineering
Web page info: https://jten.yildiz.edu.tr
DOI: 10.18186/thermal.1428999

Journal of Thermal Engineering

Research Article

Numerical investigation of the effects of the bronchial stenosis on airflow in human respiratory tract

Ufuk DEMİR[1,*], Celal SATICI[2], Filiz KOŞAR[2], Hasan GÜNEŞ[1]

[1]Department of Mechanical Engineering, Istanbul Technical University, Istanbul, 34437, Türkiye
[2]Yedikule Hospital for Chest Disease and Thoracic Surgery Health Sciences University, Istanbul, 34020, Türkiye

ARTICLE INFO

Article history
Received: 24 September 2022
Revised: 03 March 2023
Accepted: 12 March 2023

Keywords:
Computational Fluid Dynamics (CFD); Bronchial Stenosis; Airflow in the Human Respiratory Tract. Computed Tomography; Patient-Specific Simulation

ABSTRACT

Obstructive lung diseases are slowly progressing diseases that are characterized by a narrowing of airway diameter and make it harder to breathe. Although obstructive lung diseases have a high mortality rate, there are many clinical methods for early diagnosis such as impulse oscillometry, thorax computed tomography scans, and pulmonary function tests. The objective of this study is to investigate the effects of obstructions in main bronchitis on the airflow pattern and provide a better understanding to flow characteristics in healthy and obstructed (bronchial obstructions) human airways throughout a tidal breathing pattern. Seven-generation lung airway model of a healthy person was reconstructed from computed tomography (CT) images and additional models were created artificially for investigation of how obstructed airways affect flow characteristics, flow rate, tidal volumes, and air distributions. A person-specific non-uniform pressure inlet boundary condition for 12 breaths per minute was created as a time-dependent pressure profile and implemented in FLUENT software as a macro for distal airways and atmospheric pressure outlet boundary condition defined at the trachea exit. Numerical simulations were carried out in SST k-w turbulence model and validated with an experimental study. Various flow properties such as lobar distribution rates, maximum flow rate changes, and airflow characteristics at different flow rates (quiet breathing-15 L/min and intense activity level-60 L/min) in the carina region, mid-trachea and sagittal section of the trachea were obtained in the human respiratory tract by computationally. The results show that regardless of flow rate, the airflow characteristics are similar for healthy models and models with various stenosis grades during inhalation. In terms of maximum flow rate drop, for both inspiration and expiration phases 16%, 45%, and %80 decreases were observed in OM-I, OM-II, and OM-III, respectively. In line with the decrease in maximum flow rate similar drop, percentages were obtained for tidal volumes. Besides, with the increase of stenosis grade, the inhaled air volume distribution to the right and left upper lobes decreased between 15%-95%.

Cite this article as: Demir U, Satici C, Koşar F, Güneş H. Numerical investigation of the effects of the bronchial stenosis on airflow in human respiratory tract. J Ther Eng 2024;10(1):21−35.

***Corresponding author.**
*E-mail address: ufukdemir@itu.edu.tr

This paper was recommended for publication in revised form by Ahmet Selim Dalkılıç

INTRODUCTION

With the increase in average life expectancy due to the developing diagnosis and treatment methods, there has been an increase in respiratory system diseases in the context of chronic diseases. Lung diseases are among one the most serious health problems in the world, as it causes about one-sixth of the deaths in the world today [1].

Intensive use of tobacco products, genetic factors, and air pollution are considered important etiologic factors that lead to the development of lung diseases There are three main types of lung diseases including airway, parenchymal and circulatory disorders. Among them, airway diseases such as asthma, COPD, and bronchiectasis affect the respiratory tract directly and cause bronchial obstruction. Since this group of diseases could have fatal consequences, simple and early diagnosis is very crucial. Among the target receptors of an inhaled agent, beta-adrenergic receptors are mainly located in distal airways [2], whereas muscarinic receptors were in proximal airways [3]. In line with that, the localization of the obstruction is also important for clinicians to decide on the appropriate inhaled agent. Impulse oscillometry has been used to detect the localization of the obstruction by measuring the resistance [4]. However, this diagnostic tool has not commonly used in many outpatient clinics. Instead, the localization of the obstructed airways could be detected by using thorax computed tomography scans. In addition to the clinical methods, CFD simulations are potentially useful tools to support clinical predictions and there has been extensive application of CFD techniques in biomedical applications [5] as in other fields [10]. Many experimental and numerical studies have been carried out for the treatment of lung diseases, to determine the points where inhaled drugs can affect the respiratory system, and to observe the effects of various respiratory tract disorders on the current flow characteristics in the bronchi and bronchioles. However, since the human airway tree includes a complex asymmetric branching pattern, it is very difficult to obtain and study a fully realistic lung model. In many previous studies, mathematical-anatomical models developed by Weibel, Kitaoka, and Schmidt have been used due to the complex lung structure and technological deficiencies [11-13]. The Weibel model, which is symmetrical and has specific measures for each branch and bifurcation angle, is one of the most used mathematical models in numerical studies. [14,15]. To simulate airflow in the entire lung geometry, a combination of the Weibel and Kitaoka truncated model has been used by Tena et al. [16].

In addition to the Weibel model, the asymmetric Horsfield and Schmidt models have also been used in several studies [17,18]. With the development of medical imaging methods (Computed Tomography-CT, High-Resolution Computed Tomography-HRCT, and Magnetic Resonance Imaging, MRI) and computer technology, patient-specific models obtained by segmentation of CT images and CT-based airway models and hybrid models (mathematical model plus CT-based airway model) took place in numerical and experimental studies [19-20].

In this study, we investigated the effects of bronchial stenosis on the human respiratory tract which has not been studied in detail in previous studies.

Unlike many studies in the literature, realistic patient-specific transient pressure inlet boundary conditions were used in numerical simulations. With this respect, a healthy model was reconstructed from 58-year-old Caucasian male CT images which were in DICOM (Digital Imaging and Communications in Medicine) format, then seven more models with grade I (25 % obstruction), grade II (50 % obstruction) and grade III (%75 obstruction) stenosis [21] on the bronchus were created.

MATERIALS AND METHODS

Healthy Model Construction

To create a real human respiratory tract model, the medical software package Mimics 21 and 3D Modeling software 3-Matic (Materialise, Leuven, Belgium) were used to segment CT images of the 58 years old male adult (BMI: 23.5 kg/m^2) without any history of respiratory disease. 223 CT scans were obtained in the axial plane and one slice is 512 pixels with a pixel spacing of 0.45 mm. After the segmentation of CT images, the CAD model is imported into 3-Matic software to smooth the surface and create a surface mesh. The resulting seven-generation CT-based fluid domain (right) which consists of 25 outlets and lung lobes at total lung capacity (TLC) with respiratory tract (left) is depicted in Figure 1.

Figure 1. Lung lobes and respiratory tract after segmentation.

	Gen.	Center Line Length (mm)	Mean Diameter (mm)	Mean Cross Sectional Area (mm2)	Circularity (Cr)	Hydraulic Diameter (mm)	Perimeter (mm)
Trachea	0	142	19,8	308	0,94	19	66
RMB	1	21,14	17,4	240	0,96	17	57
LMB	1	59	14,9	175	0,98	15	47,8
	2	29,2	9,6	73	0,94	9	32
	3	24,3	5,86	27	0,92	5	20
	4	17,85	7,7	47	0,93	7	26
	5	18,4	3,74	11	0,90	3	13
	6	12,8	4,06	13	0,91	4	14

Figure 2. Physical specifications of the model.

Figure 2 demonstrates the physical dimensions of an obtained model like circularity ratio, center line length, perimeter, and mean dimensions of each generation.

Construction of Obstructed Models

There are different types of airway stenosis such as tracheal stenosis, bronchial stenosis, tracheobronchial stenosis, subglottic stenosis, etc. Stenosis can be defined as the permanent narrowing of the airway tubes which are made of muscle and connective mucus membranes. Although there is no adequate classification in the literature regarding airway stenosis, the classification created by Freitag et al. [21] was used. Within the scope of this study, we created obstructed models from a healthy person (fluid domain) to simulate bronchial stenosis. To obtain grade I, grade II, and grade III stenosis models, we decreased both main bronchi diameters by %25, %50 and %75 respectively. Figure 4 presents the obstruction levels that created both main bronchi. HM, OM-I, OM-II and OM-III abbreviations are used for the healthy model, a model with grade I stenosis, a model with grade II stenosis, and a model with grade III stenosis, respectively.

Mesh Generation and Independency Test

The fluid domain which was prepared for numerical simulations is exported to FLUENT format and imported into ANSYS Fluent-Meshing (ANSYS, Inc., Canonsburg, PA) where tetrahedral surface meshes were converted to polyhedral volume meshes. Polyhedral volume mesh type was used to obtain exceptional mesh quality leading to improved numerical stability and lower cell size to get a more accurate solution. Mesh refinement is increased at the trachea inlet, distal bronchioles outlet, and obstructed regions and the mesh quality is evaluated by the skewness value. The maximum skewness value is assumed to be lower than 0.7 for all models. The five inflation layers with a growth rate of 1.2 were applied to the respiratory tract walls to capture the boundary layer region accurately. Figure 4 shows the computational domain at the sagittal section of the trachea.

To obtain reliable and accurate numerical results, intensive mesh independence tests have been performed with constant pressure inlet and outlet boundary conditions for all models. The simulations were carried out for the seven

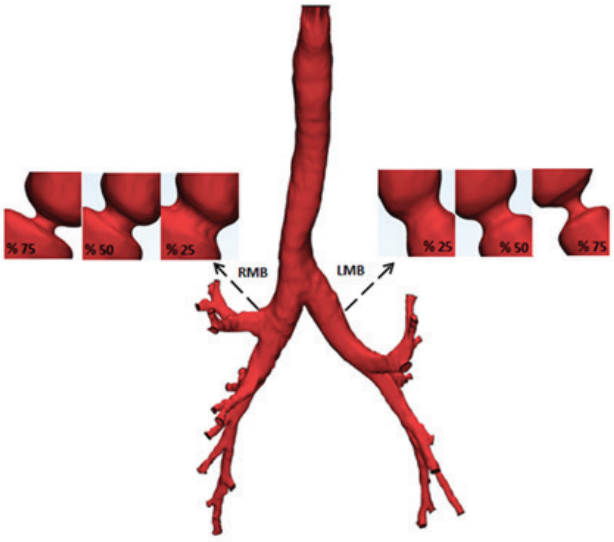

Figure 3. Grade I, II, and III stenosis on the healthy model.

Figure 4. The polyhedral mesh and boundary layers in the trachea.

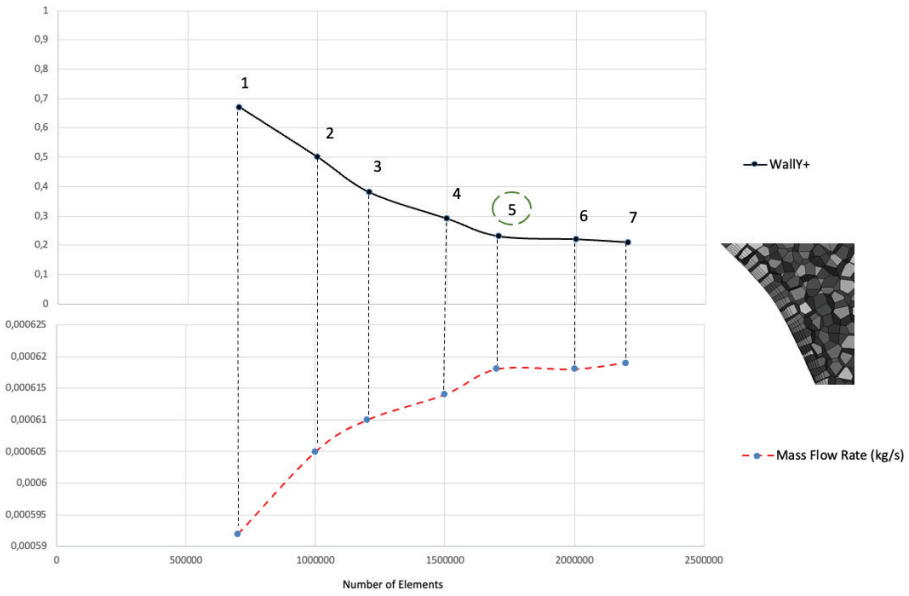

Figure 5. Mesh independency test.

different meshes and mass flow rates at the trachea exit and wall Y+ were studied.

As can be seen from Figure 5, mesh number 5 points 0,23 for wallY+ and 0,000618 kg/s for mass flow rate and there is no significant change in these values after this point. Therefore, a 1.7 M mesh size was selected for numerical simulations. The mesh independence tests for the other models were conducted in the same conditions.

Boundary Conditions

Two important parameters affect the airflow in the respiratory tract in numerical simulations, model geometry, and boundary conditions. To obtain more accurate results we used patient-specific transient pressure boundary conditions instead of traditional uniform velocity and pressure boundary conditions. For sedentary activity level (15 L/min) airway resistance was calculated by using Ohm's law (1).

$$R_{airway} = \frac{P_{atm} - P_{alv}\ (cm\,H_2O)}{\dot{V}(lt/s)} \quad (1)$$

For quiet breathing also known as eupnoea, alveolar pressure was taken to be 1 cm H_2O at the expiration phase and -1 cm H_2O at the inspiration phase [22].

After specifying the required pressure drop between trachea inlet and distal airway outlets for the desired volumetric flow rate, time-dependent pressure inlet boundary conditions for a respiratory cycle of 5 s (12 breaths per minute) were created as a time-dependent profile and implemented in FLUENT software as a pressure profile macro for distal airways. Time-dependent pressure profiles for inhalation and exhalation phases are given in Eqs 2 and 3 as 4^{th}-degree polynomial equation form.

0 s < Current time < 2 s

$$P = 2.4 * t^4 - 8.57 * t^3 + 12{,}9 * t^2 - 10{,}8 * t + 0{,}2 \quad (2)$$

2 s < Current time < 5 s

$$P = -0.4 + 5.94 * t^3 - 33{,}2 * t^2 + 81{,}1 * t - 70{,}1 \quad (3)$$

The obtained profile had an inspiration/expiration ratio of 1:1,5. Figure 7 shows pressure boundary conditions for two respiratory cycles (inhalation and exhalation) at the distal airways for various flow rates (15, 30 and 60 L/min.). These boundary condition graphs were obtained by using equations (2) and (3). Meanwhile, atmospheric pressure outlet boundary conditions were defined at the trachea exit and no-slip conditions were implemented at the wall.

In the current study, for quiet breathing, the subject's tidal volume ranges between 462-616 mL (6-8 mL per kg) [23] and 509 mL tidal volume obtained with the created pressure profile. All simulated OM models used the same inlet pressure (25%–75% obstruction). Reynolds, Strouhal, and Womersley numbers are three dimensionless numbers that can be used to describe the flow characteristic. Reynolds number is the ratio of inertial forces to viscous forces within a fluid and is given by

$$Re = \frac{\rho U D}{\mu} \quad (4)$$

Model	Re	
	Trachea	Distal Airways
HM	2315	280
OM-I	1917	215
OM-II	1362	177
OM-III	463	148

Figure 6. Re numbers in the trachea and distal airways at a peak flow rate.

where U (m/s), ρ (kg/m^3), D (m), and μ (Pa s) are velocity, fluid density, characteristic length (diameter), and dynamic viscosity respectively.

Figure 6 shows the mean Re numbers both in the trachea and distal regions for all models. With the increasing obstruction degree significant decrease in Re numbers, both in the trachea and distal regions can be seen in Figure 6.

Strouhal number is the ratio of inertial forces due to the acceleration of the flow to the inertial forces. U, D, and f are velocity (m/s), characteristic length (m), and frequency (1/s) in Eq. 3, respectively

$$St = \frac{fD}{U} \tag{5}$$

The Womersley number (α) indicates the relative importance of inertial and viscous forces and is used to determine the significance of the unsteadiness in the flow.

In case α is less than 1, the flow has time to become fully developed during each cycle and there is a parabolic velocity profile. At higher values of α (around 10), inertial forces begin to influence the flow, and this causes a flat or plug velocity profile. Since the maximum Womersley and Strouhal numbers are 5.88 and 0.01 respectively, the flow can be assumed as quasi-steady [24]. A workstation with 32 Gb RAM, 3.4 GHz CPUs, and 16 processor cores was utilized for the CFD calculations.

Numerical Methods

The airflow was assumed to be fully developed and incompressible. So, for incompressible flow

and Newtonian fluid, conservation of mass, and time-dependent Navier-Stokes equations were denoted by equations (6) and (8) respectively.

$$\nabla\rho\vec{V} + \frac{\partial\rho}{\partial t} = 0 \tag{6}$$

$$\nabla = \imath\frac{\partial}{\partial x} + \jmath\frac{\partial}{\partial y} + \vec{k}\frac{\partial}{\partial z} \tag{7}$$

$$\rho\frac{D\vec{V}}{dt} = \rho g - \nabla p + \mu\nabla^2\vec{V} \tag{8}$$

where P, $\vec{V}$ and g are pressure, velocity vector, and gravity vector, respectively.

Even during quiet breathing, the airflow characteristics in the respiratory tract are very complex due to flow instabilities caused by asymmetrical patterns and morphological

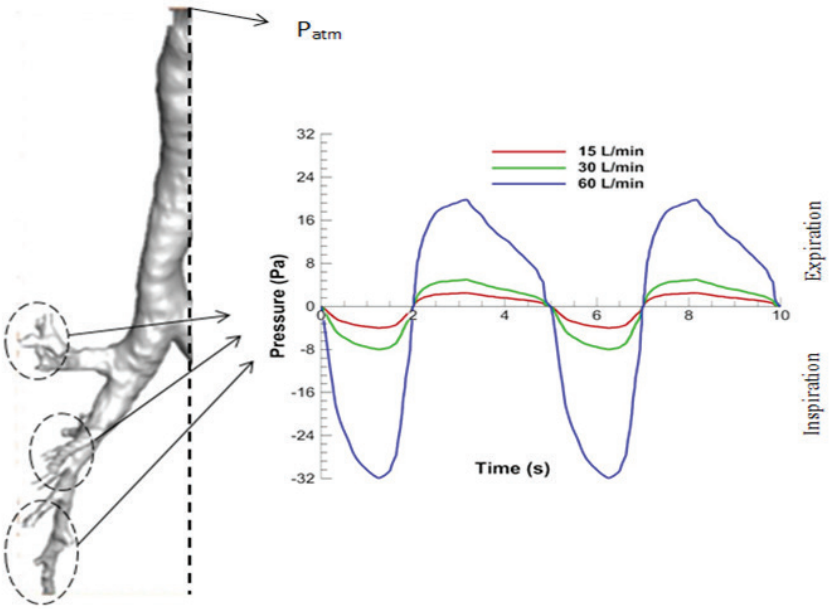

Figure 7. Pressure boundary conditions at different flow rates.

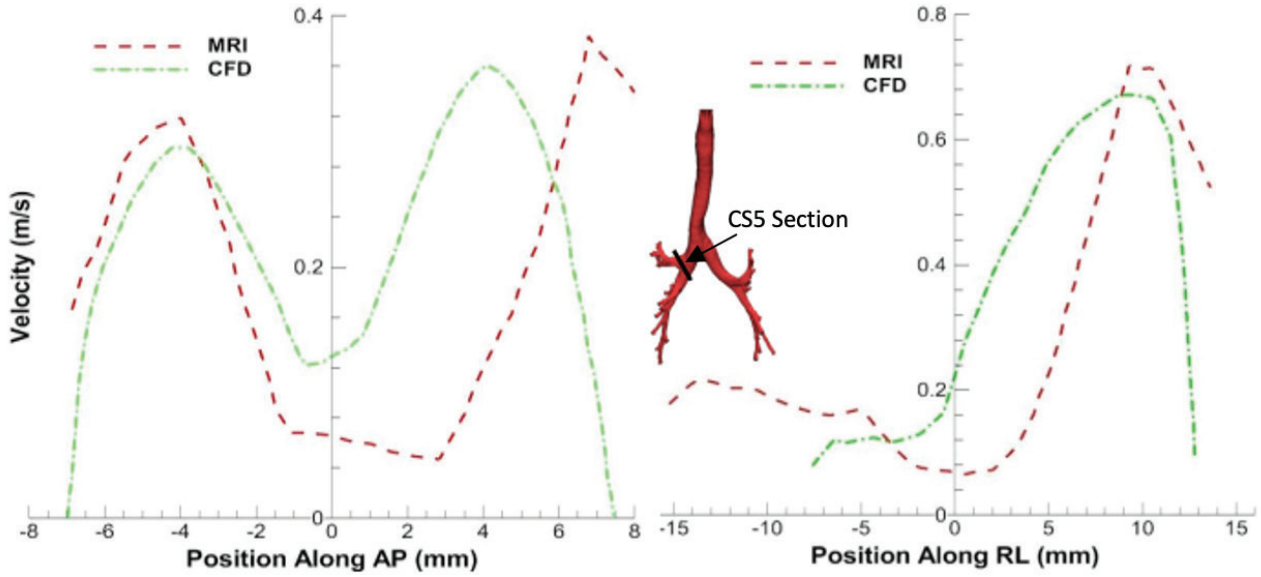

Figure 8. The velocity profiles at the CS05 section.

irregularity. Since the blending function (F1) equals "1" near the wall and gives a better understanding of near-wall behavior of flow, numerical simulations were carried out in SST k-w turbulence model. Shear Stress Eqs. for the SST k-w model are [25]:

$$\frac{\partial}{dt}(\rho k) + \frac{\partial}{\partial x_i}(\rho k u_i) = \frac{\partial}{\partial x_j}(\Gamma_k \frac{\partial k}{\partial x_j}) \quad (9)$$

$$+G_k - Y_k + S_k + G_b$$

and

$$\frac{\partial}{dt}(\rho \omega) + \frac{\partial}{\partial x_i}(\rho \omega u_i) = \frac{\partial}{\partial x_j}(\Gamma_\omega \frac{\partial \omega}{\partial x_j}) \quad (10)$$

$$+G_\omega - Y_\omega + S_\omega + D_\omega + G_{\omega b}$$

In equations 9 - 10, G_k represents the TKE production and G_ω is the generation of ω. T_k and T_ω stand for the effective diffusivity of k and ω, Y_k and Y_ω represent the turbulence dissipation rate of k and ω. D_ω symbolizes the cross-diffusion term, S_k-S_ω are user-defined source terms, and G_b- represents the buoyancy effects. The solver algorithm was selected COUPLED which is preferred for transient flow simulations to obtain accurate results. A residual of 10^{-5} is taken as the convergence criterion of continuity and momentum equations. The continuity and momentum equations have been discretized using second-order upwind schemes. For the transient simulations, time step size and time step number were selected as 0.001s and 5000, respectively. The working fluid, the air is assumed to be a Newtonian and the density and viscosity of air are 1.225 kg/m^3 and 1.7984x10^{-5} kg/m-s respectively.

Validation of Fluid Domain

To validate our model, velocity profiles that resulted from CFD simulations at the CS05 (bifurcation point of right main bronchi) section, were compared with the profiles obtained by De Rochefort et al. using Magnetic Resonance Imaging (MRI) technique on a human respiratory tract model. The same boundary conditions (flow rate of 269 mL/s) were adopted in the numerical study as in Rocheford et al. [26].

Figure 8 illustrates velocity profiles at the right main bronchi along the anterior to posterior and along the right to left positions. As can be seen in Figure 8, the velocity profiles obtained in the CS5 cross section are consistent with the MRI measurement, but the velocity values at certain locations are higher (maximum velocity points deviation is 6% for both AP and RL directions) in the CFD study. This difference comes from individual morphological variations of the two different models. Since the diameter of the CS05 section in the current model is smaller than De Rocheford's model, the decreased cross-section area at the constant volumetric flow rate increases the average velocity value in that section. So, we used the Re analogy to reduce obtained velocity values.

RESULTS AND DISCUSSION

In the present study, numerical simulations were performed on one healthy and seven artificially obstructed models with grade I-II-III bronchial stenosis. First of all the

numerical analyses were performed on the healthy model, after, the effects of the obstructions on the respiratory tract were investigated at different flow rates. Tidal volume changes, lobar distribution of inspired air, and changes in airflow characteristics were compared. Effects of tracheal inclination and glottis region constriction at the mid-trachea section for 15 L/min and 60 L/min flow rates can be seen in Figure 9.

The characteristic of the airflow pattern is similar in both flow rates. Owing to the angle of the trachea slope, inhaled air flowed along the anterior wall of the trachea and a secondary flow pattern appeared on the posterior side of the respiratory tract during inhalation. The airflow was less disturbed because of the lower airway resistance, and this led to a more uniform flow field, so the maximum velocity was smaller during exhalation than that during inhalation. Figure 10 shows the maximum flow rate changes in obstructed models according to the healthy model. As can be seen from graph bars in Figure 10, the inspiration max flow rate decreased more than the expiration max flow rate due to the grade I stenosis only in the LMB and the models with 50% and higher stenosis grades while it occurred vice versa in the RMB and both OM-I models.

With the increase of flow rate of 15 L/min to 60 L/min, airflow became more complicated and the drop percentages of maximum flow rates at inspiration and expiration were increased prominently for all models. At 60 L/min flow rate, the inspiration max flow rate decreased more than the expiration max flow rate for all models except the model with grade I stenosis only in the RMB. It was observed in the study that has been conducted by Lin et al. [27] that with the 50 % decrease at the cross-section area due to the stenosis, the airway resistance increased by about 45 % which is in line with this study, it can be seen from Figure 10 that in the OM-II (50 % obstructed) model max flow rates at both inhalation and exhalation dropped by about 50 %.

Figure 11 gives inhaled air volumes for two different flow rates, 15 L/min, and 60 L/min respectively. For both flow rates, tidal volumes decreased by doubling with increasing stenosis grade and it was seen that the least decrease occurred in the model with grade I stenosis only in the right main bronchus in Figure 12. The distribution of inhaled air rates throughout the lung lobes for each model was given in Figure 13.

With an increased obstruction ratio more air near the tracheal wall with a slow velocity is inhaled into the right and left upper lobes, while the central flow enters the right middle, lower, and left lower lobes. This phenomenon caused the amount of air inhaled into the RUL and LUL to decrease while more air flow to the RML, RLL, and LLL. Main lobar distribution rates between the right lung and

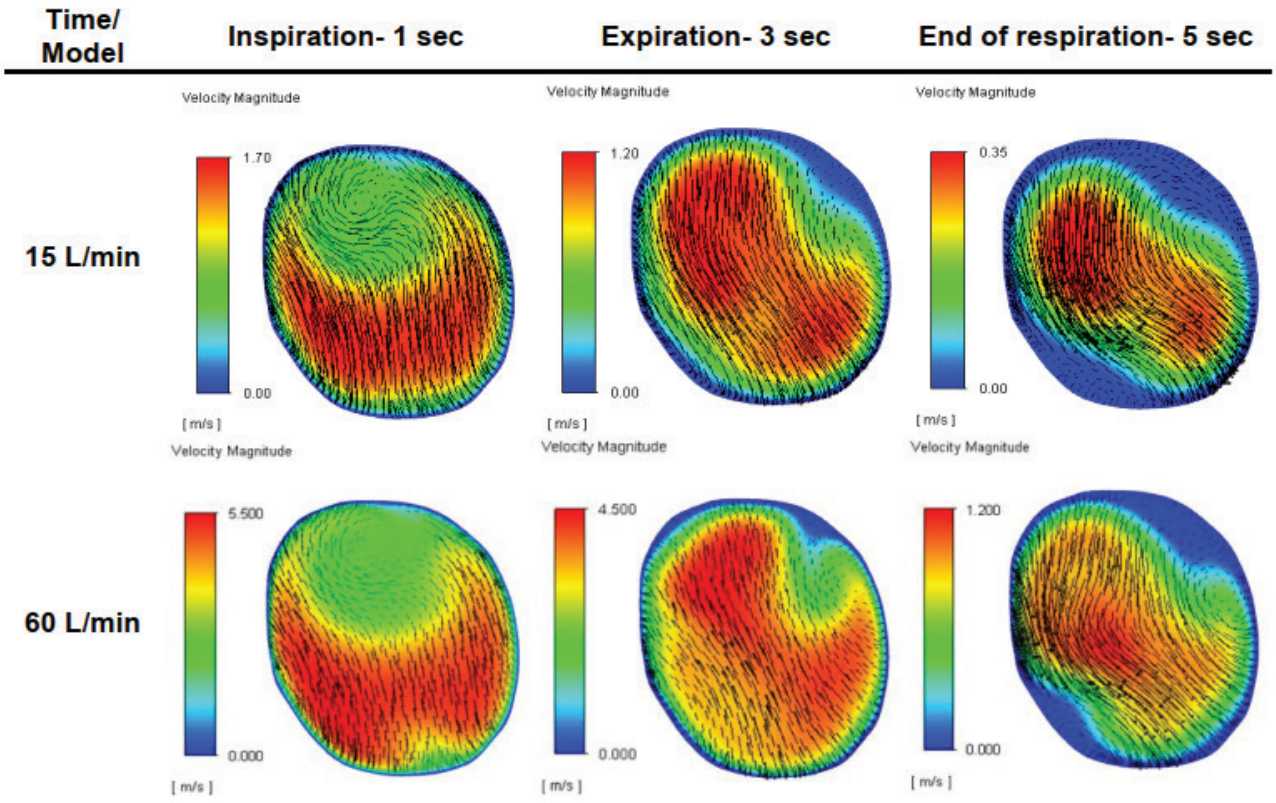

Figure 9. The velocity contours and vectors at the mid-trachea section for HM.

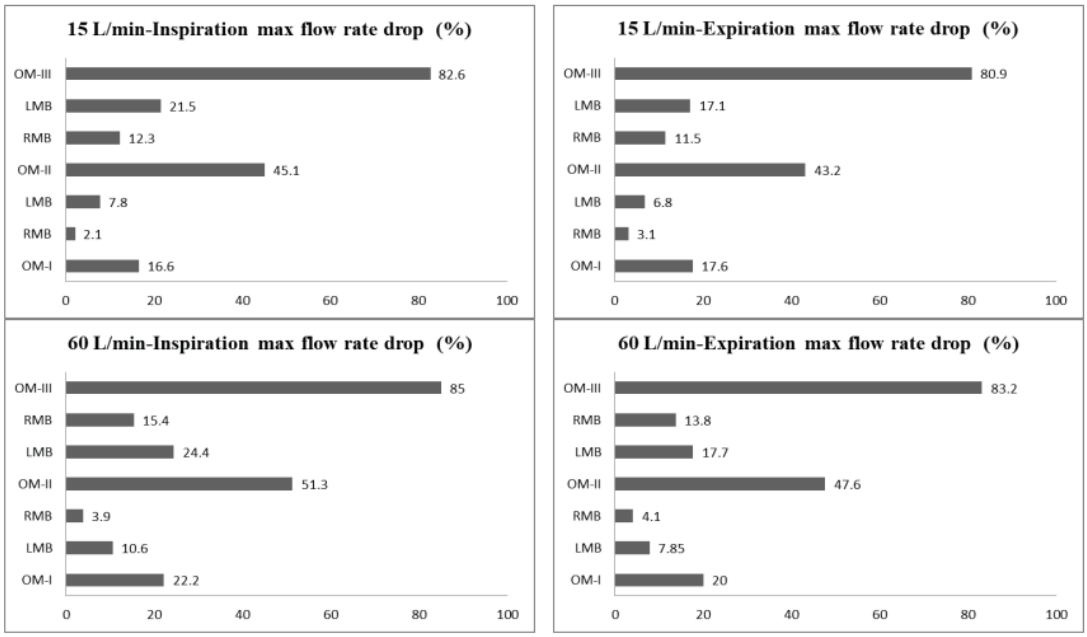

Figure 10. Max flow rate drop rates for all models.

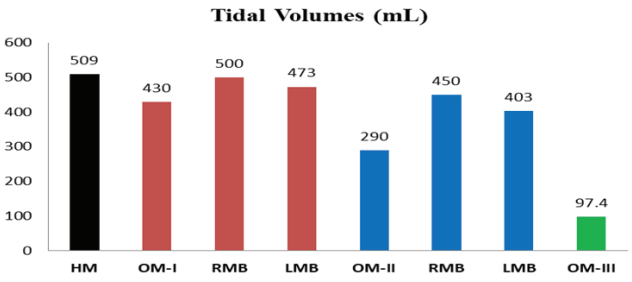

Figure 11. Inhaled air volumes at different flow rates.

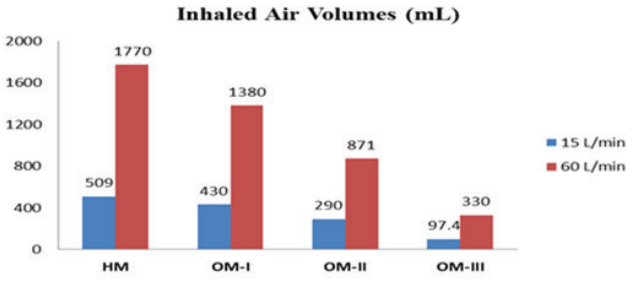

Figure 12. Tidal volumes for all models at 15 L/min flow rate.

the left lung are almost equal for the healthy model (49.2 % RL, 50.8 % LL), but there is an increase in the amount of inhaled air moving to the right lung (60.7 % RL, 39.3 % LL for OM-III) proportional to the stenosis level.

Figure 14 demonstrates velocity contours with velocity vectors in the mid-trachea region at different time points. For the profiles of velocity distribution, especially for the area covered by maximum velocity, similar trends are found across all the models at peak inhalation time (1s). At inspiration, the main streamlines located anterior (front side of the tracheal tube) walls of the trachea regardless of the occurrence of bronchial stenosis due to the morphological nature (natural slope) of the respiratory tract. At expiration, with the occurrence and increase of stenosis, the secondary flow velocity vectors appear near the left wall. The secondary flow is directed from the left side to the right side of the trachea and pushed the center streamlines toward to right wall.

While the air coming from daughter branches of the trachea (right and left main bronchus) mixed prominently in the HM carina region, the air streamlines from main bronchial tubes formed two separate center flows in the models with stenosis as can be seen in Figure 15. Due to the stenosis regions on the main bronchi, the airflow passing constricted zone was accelerated, entering the trachea region through carina, and then mixed each other. So, the jet-like flow caused by the stenosis region made the airflow structure more complex and the flow can be described as chaotic at peak expiratory flow rate for obstructed models. Also, with increasing stenosis grade, the area covered by strong streamlines moved from the inner wall of the carina to the center of each main bronchus. Figure 16 shows recirculation zones that appear posterior wall of the trachea where the velocity was almost equal to zero, for all models during inhalation. But during the expiration condition, clear differences are visible in the axial-flow velocity patterns for

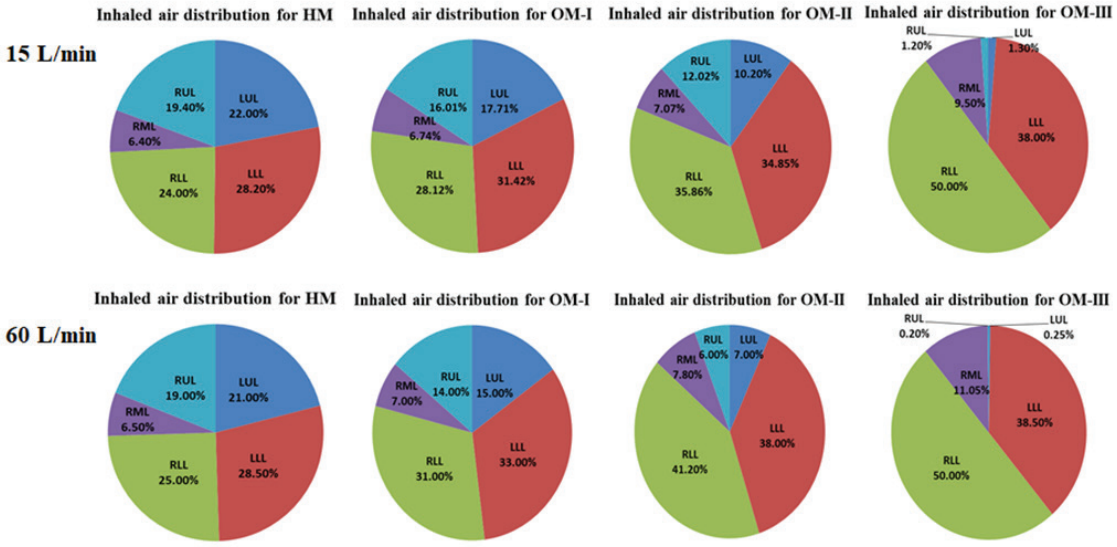

Figure 13. Inhaled air lobar distribution rates for all models.

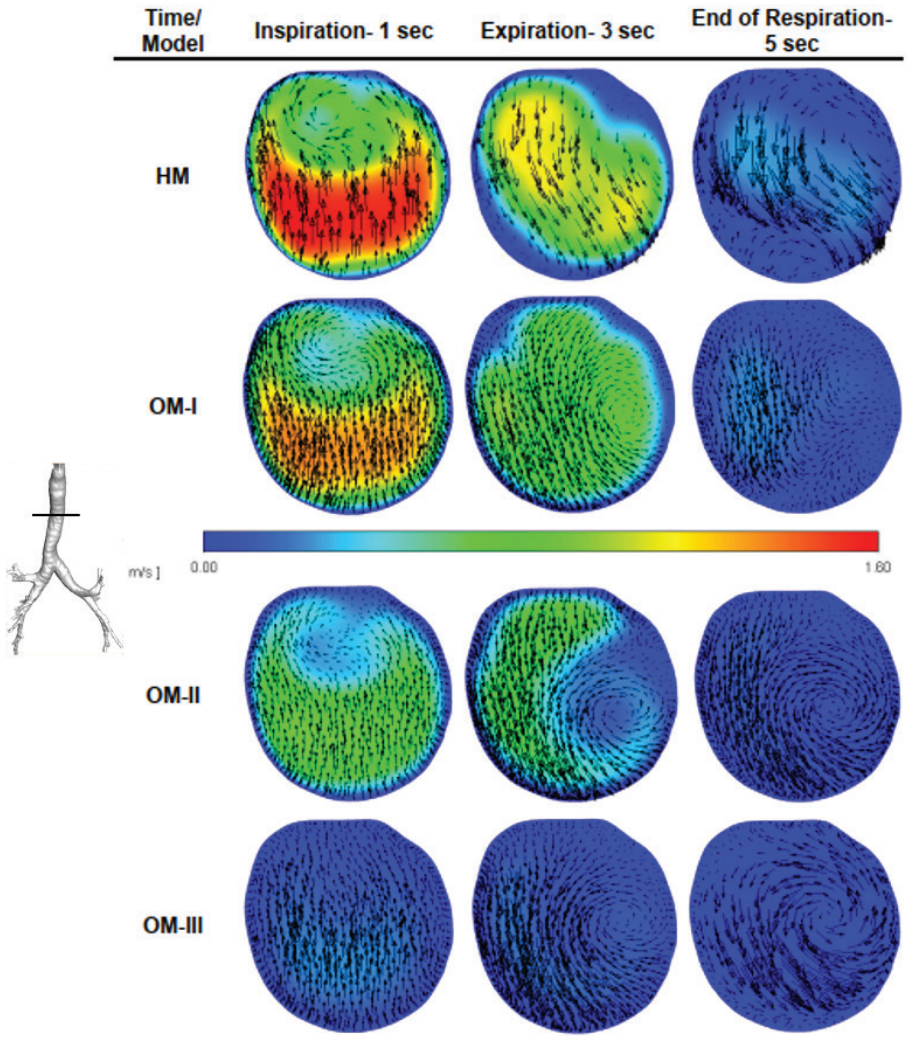

Figure 14. The velocity contours and vectors at the mid-trachea section (15 L/min).

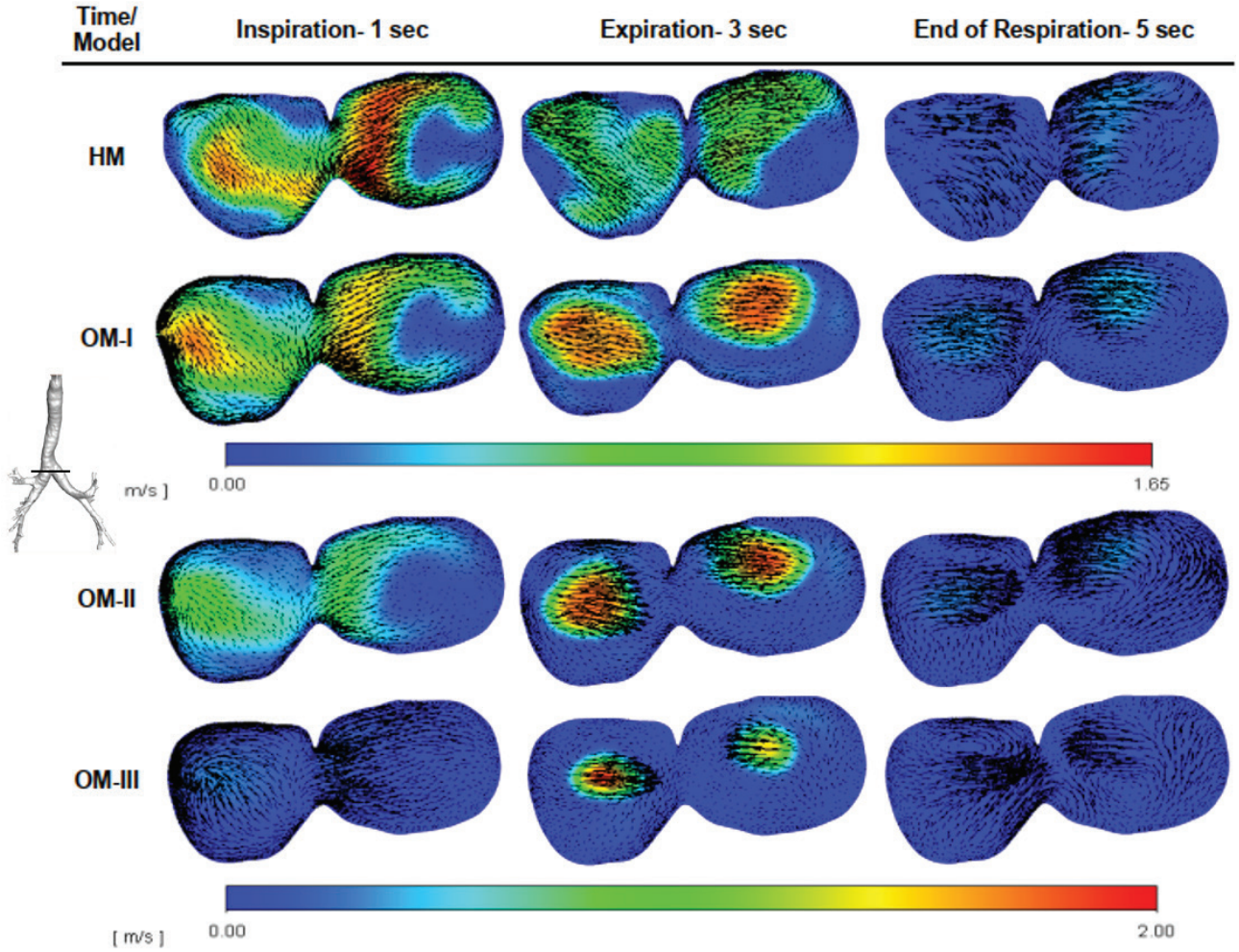

Figure 15. The velocity contours at the carina section (15 L/min).

all models. In HM, high-speed airflow in the sagittal plane appeared in the center of the trachea but no obvious airflow patterns in the axial direction appeared for obstructed models.

When the results are examined in terms of maximum velocities, for HM the flow velocity near the anterior wall is higher than that in the center and posterior walls at peak inhalation, furthermore, the positions of the streamlines are switched to the center and the maximum velocity decreased about % 30 at peak expiration. Higher flow velocity appears mostly above the carina region due to the jet-like flow, where two main bronchi streamline mix. Maximum velocities at inspiration and expiration decreased in the mid-trachea region while the maximum velocity at expiration increased by about 36 % in OM-I, 60 % in OM-II, and 80 % in OM-III at the carina region. Figure 17 shows Reynolds number and Strouhal number variations through each generation for all models using velocity data obtained from simulation results with a 15 L/min flow rate. Reynolds number at the trachea of HM is about 2315 and the transitional or turbulent flow regime appeared within the trachea and low level of turbulence through the generations.

In contrast, the Re numbers at the trachea and first two generations are higher than the critical Re value and the flow is assumed to be in a transitional or turbulent regime through these generations for obstructed models. A relatively higher Re number due to the stenosis region decreased promptly after the stenosis region through the next generations. The lowest Re number appeared in the grade III stenosis model as expected.

The inverse relation between Reynolds and Strouhal numbers can be seen clearly in Figure 17. With decreasing hydraulic diameter along the respiratory tract, both inertial forces due to the local acceleration and inertial forces due to the convective acceleration decrease. As convective acceleration is related to spacial gradients of velocity, inertial forces induced by convective acceleration decreased much more with higher stenosis levels; hence the unsteadiness of the flow is higher through each generation after the contraction point even in low Re values.

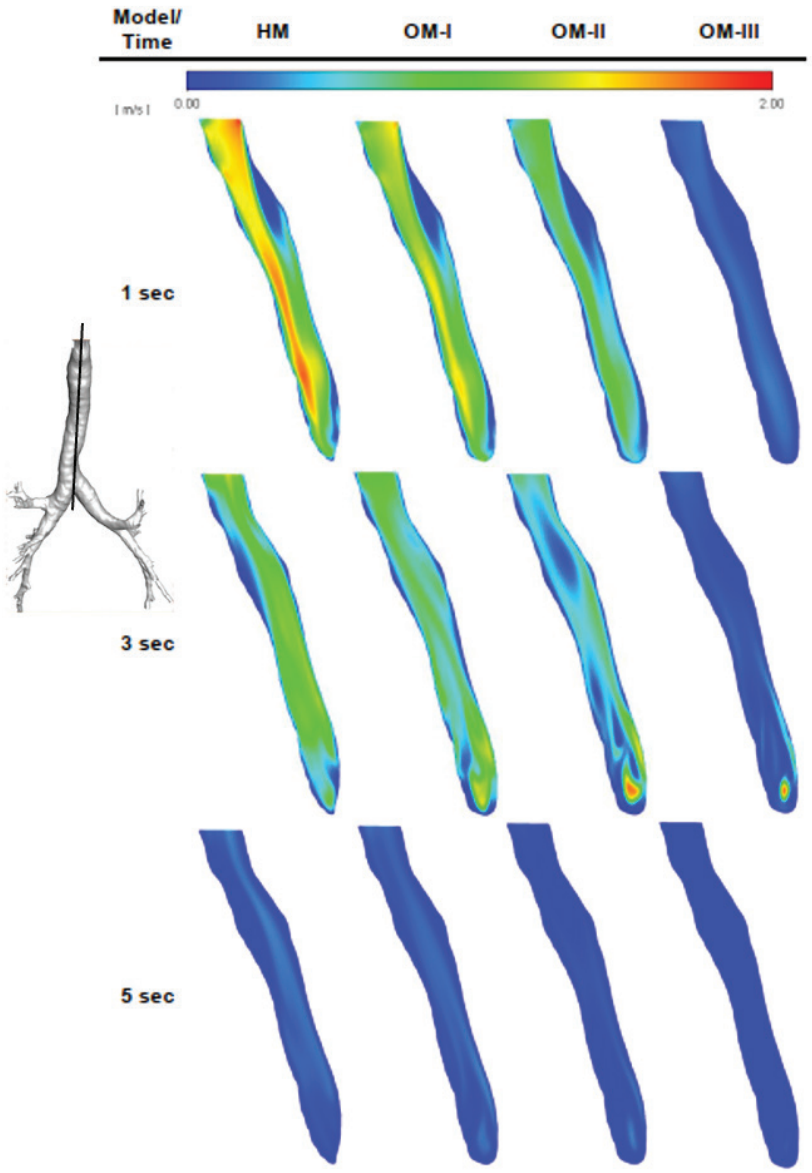

Figure 16. The velocity contours at sagittal section of the trachea (15 L/min).

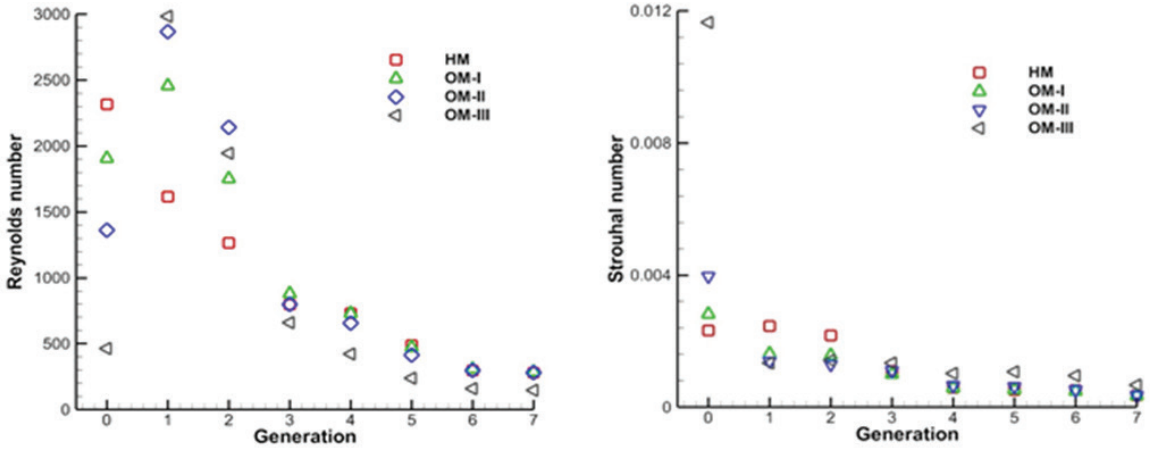

Figure 17. Re and St number variation along the generations at peak inspiration.

Effects of various lung diseases, such as tracheal bronchus, tracheal stenosis, subglottic stenosis, cystic fibrosis, and left artery sling, on the respiratory tract, were investigated numerically by using CT-based models or disease simulation models [28-30]. Presented here is the work on the human respiratory tract which was reconstructed from healthy, 58 years old non-smoking Caucasian male CT images. Seven models with various stenosis grades were obtained and airflow patterns, lobar air distribution rates, and max flow rates were compared to healthy and obstructed airways for quiet and intense activity levels. The computational simulations on healthy and obstructed fluid domains were performed at the transient flow rates of 15 L/min and 60 L/min for a full respiratory cycle, by using the SST k–ω model which has good accuracy in the treatment of the viscous near-wall region and explaining the effects of adverse pressure gradients [31]. This model was chosen in many previous numerical studies due to its close predictions to experimental results [32,33].

It was shown that with appropriate boundary conditions, CFD simulations can yield information that is similar to that obtained with experimental studies [34]. Qi et al. compared simulation results on flow patterns and air distributions by using both transient velocity profile and pressure profile and found no obvious discrepancies between the results [35]. Yin et al. [36] indicated that subject-specific boundary conditions give more accurate results than simple uniform boundary conditions compared to experimental results. Therefore, to obtain a better understanding of the airflow characteristics in the respiratory tract, numerical simulations were carried out with subject-specific pressure boundary conditions instead of traditional uniform boundary conditions in the current study. For the transient pressure profile, we calculated the airway resistance of the segmented model and maximum pressure drop value (about 4 Pa for 15 L/min flow rate) by using Ohm's law for the desired flow rate.

Turbulent laryngeal jet flow is another point to consider which is induced by the airway constriction at the glottis region. Since many numerical and experimental studies have been conducted to show the glottis effects on airflow in the tracheal tube [37,38], the position of true vocal cords is vague during breath-holding while having a CT scan [39]. Due to this obscurity, we included the only end of the glottis region in our segmented model and this part of the glottis was sufficient to accelerate the inhaled air.

At inspiration, main streamlines are located anterior walls of the trachea regardless of the occurrence of bronchial stenosis due to the morphological nature of the respiratory tract, which coincides with previous studies [40,41]. Additionally, a recirculation zone appeared on the upper posterior wall of the trachea where flow separation occurred due to the circulating backflow like the work of Heenan et al. [42]. Another factor to consider is lobar distribution rates which have an important role in drug aerosol dynamics. To obtain a better understanding of the distribution and deposition of aerosol particles in the respiratory tract, airflow characteristics have also been investigated in many numerical studies. Lambert et al. [43] concluded that there is a linear relation between the distribution of the particles and the inhaled air to the lung lobes. De Backer et al. [34] found that a large percentage of inhaled air flowed to the lower lobes than the upper lobes. Concordantly we found both the right and left lower lobes receive about 25-30 % of inhaled air while 20 % flowed to the upper lobes. With increasing stenosis grade on the main bronchi inhaled air volume to the upper lobes decreased dramatically and hence the air inhaled to the right middle and both lower lobes increased. It can be seen in Figure 12 that the least decrease occurred in the model with grade I stenosis only in the right main bronchus. It was evaluated that this was because the RMB had a larger diameter than the LMB and the same stenosis grade at the RMB did not affect the amount of inhaled air as much as LMB. In HM, the expiration flow was more uniform than the inspiration condition. But with the occurrence and increase of stenosis grade, the airflow mixed above the carina and jet-like flow induced by stenosis region turned the uniform flow structure into a more complex one. So more than one recirculation zones appeared on the sagittal section of the tracheal tube. Although the airflow characteristics and lobar distribution rates in both healthy and obstructed models are explained well in this study, there are still some limitations. We used only one healthy subject CT image and additional models with various simulated stenosis were created, large case numbers and real patient models are needed for consequential work. A complete airway model could not be segmented and used, due to the medical imaging technology limitations in the numerical simulations so the flow pattern may be influenced by the lack of distal airways. In this retrospective study, we used predicted values for transient pressure boundary conditions of this subject, usage of a complete personalized respiration waveform and measured values can give more realistic results. In future studies, creating a hybrid complete respiratory tract model and forming subject-specific forced expiration pressure boundary conditions to obtain important PFT (Pulmonary Function Test) parameters like FEV1, FEV3, PEF, etc. in CFD studies and comparing with real PFT results would be more useful in clinical applications.

CONCLUSION

To improve our understanding of the airflow characteristics in the respiratory tract, numerical simulations were carried out with subject-specific pressure boundary conditions while most previous investigations have used traditional uniform boundary conditions. Results of numerical studies, which were performed under different flow rates, show that;

- Velocity profiles in the respiratory tract depend on the airway geometry far more than the Re number.
- Hence obtained airflow characteristics in the respiratory tract had similar patterns during inhalation for all models.
- Airway resistance increases with various stenosis grades and patients with bronchial stenosis disease have shortness of breath due to increased airway resistance and difficulty exhaling the inhaled air from the lungs.
- Because of stenosis on the main bronchi, exhaled air gets weaker and comes out more slowly in obstructed models.
- Inhaled air distribution to the upper lobes decreases with the increasing stenosis grade and the air that flows to the upper lobes gets very thin at above 50 percent obstruction.

In conclusion, we conclude that when airway stenosis increases, the upper lobes are poorly ventilated. Based on this statement, if we will plan a lung volume reduction surgery in a patient with lower lobe dominant hyperinflation, we may not get an expected respiratory function increase in pulmonary function test and clinical improvement. Because residual predominantly upper lung lobes do not contribute as much as we expected in these patients. In line with this, thoracic surgery for this patient should be considered regarding this study's results.

NOMENCLATURES

D	Diameter (m)
f	Frequency (1/s)
$\dot{m}$	Mass flow rate
P	Pressure (cmH_2O)
U	Velocity (m/s)
V	Volume (mL)
$\dot{V}$	Volumetric flow rate (L/min)

Greek symbols

ρ	Density (kg/m^3)
μ	Dynamic Viscosity (kg/m.s)

Abbreviations

CT	Computed Tomography
CFD	Computational Fluid Dynamics
CPU	Central Process Unit
FEV	Forced Expiration Volume
GHz	Giga Hertz
HM	Healthy Model
LL	Left Lung
LLL	Left Lower Lobe
LUL	Left Upper Lobe
LMB	Left Main Bronchi
OM	Obstructed Model
PEF	Peak Expiratory Flow
PFT	Pulmonary Function Test
RAM	Random Access Memory
RLL	Right Lower Lobe
RML	Right Middle Lobe
RMB	Right main Bronchi
RUL	Right Upper Lobe
RL	Right Lung

ACKNOWLEDGMENTS

The authors would like to thank "Materialise" for providing a trial version of the Mimics software package for the use of the segmentation process.

AUTHORSHIP CONTRIBUTIONS

Authors equally contributed to this work.

DATA AVAILABILITY STATEMENT

The authors confirm that the data that supports the findings of this study are available within the article. Raw data that support the finding of this study are available from the corresponding author, upon reasonable request.

CONFLICT OF INTEREST

The author declared no potential conflicts of interest with respect to the research, authorship, and/or publication of this article.

ETHICS

There are no ethical issues with the publication of this manuscript.

REFERENCES

[1] Gibson J, Loddenkemper R, Sibille Y, Lundback B, Fletcher M. Lung health in Europe, facts and numbers. Europe Lung White Book. 2013.

[2] Mutlu GM, Factor P. Alveolar epithelial beta2-adrenergic receptors. Am J Respir Cell Mol Biol 2008;38:127−134. [CrossRef]

[3] Buels KS, Fryer AD. Muscarinic receptor antagonists: effects on pulmonary function. Handb Exp Pharmacol 2012;208:317−341. [CrossRef]

[4] Bickel S, Popler J, Lesnick B, Eid N. Impulse Oscillometry Interpretation and Practical Applications. Chest 2014;146:841−847. [CrossRef]

[5] Kızılırmak E, Turgut O. Bio-heat transfer in cancer treatment using cryo-freezing method. J Therm Eng 2021;7:1885−1897. [CrossRef]

[6] Shugata A, Erwin S, Ahmad FI, Muhammad HH, Zahir H. Thermal Resistance and Pressure Drop Minimization for a Micro-gap Heat Sink with Internal Micro-fins by Parametric Optimization of Operating Conditions. CFD Lett 2021;13:100−112. [CrossRef]

[7] Ali MH, Sapit AB, Abed QA, Abbas MS, Saheb BA, Muhammed N, et al. Thermal Performance of Corrugated Solar Air Heater Integrated with Nanoparticles to Enhanced the Phase Change Material (PCM). Int J Mech Mechatron Eng 2019;19.
[8] Hasen SS, Kareem RS, Ali HA. Mathematical Analysis of Peristaltic Pumps for Fene-P model subject to Hall and Joule impact. Iraqi J Sci 2022;63:3141−3152. [CrossRef]
[9] Zedan AJ, Faris MR, Bdaiwi AK. Performance Assessment of Shirin Earth Dam in Iraq Under Various Operational Conditions. Tikrit J Eng Sci 2022;29:61−74. [CrossRef]
[10] Shugata A, Erwin S, Ahmad FI, Muhammad HH, Zahir H. Thermal Resistance and Pressure Drop Minimization for a Micro-gap Heat Sink with Internal Micro-fins by Parametric Optimization of Operating Conditions. CFD Lett 2021;13:100−112. [CrossRef]
[11] Han B, Hirahara H. Effect of Gas Oscillation Induced Irreversible Flow in Transitional Bronchioles of Human Lung. J Flow Control Meas Vis 2016;4:171−193. [CrossRef]
[12] Schmidt A, Zidowitz S, Kriete A, Denhard T, Krass S, Peitgen HO. A digital reference model of the human bronchial tree. Comput Med Imaging Graph 2004;28:203−211. [CrossRef]
[13] Kitaoka H, Takaki R, Suki B. A three-dimensional model of the human tree. J Appl Physiol 1999;87:2207−2217. [CrossRef]
[14] Walters DK, Luke WH. A Method for Three-Dimensional Navier-Stokes Simulations of Large-Scale Regions of the Human Lung Airway. J Fluids Eng 2010;132:422−429. [CrossRef]
[15] Yang XL, Liu Y, Luo HY. Respiratory flow in obstructed airways. J Biomech 2006;39:2743−2751. [CrossRef]
[16] Tena AF, Fernandez J, Alvarez E, Casan P, Walters DK. Design of a numerical model of lung by means of a special boundary condition in the truncated branches. Int J Numer Meth Biomed Eng 2016. [CrossRef]
[17] Sul B, Wallqvist A, Morris MJ, Reifman J, Rakeesh V. A Computational Study of the Respiratory Airflow Characteristics in Normal and Obstructed Human Airways. Comput Biol Med 2014;52:130−143. [CrossRef]
[18] Gemchi T, Ponvayin V, Chen H, Collins R. CFD Simulation of Airflow in a 17-Generation Digital Reference Model of the Human Bronchial Tree. Ser Biomech 2007;23:2047−2054. [CrossRef]
[19] Choi S, Miyawaki S, Lin CL. A Feasible Computational Fluid Dynamics Study for Relationships of Structural and Functional Alterations with Particle Depositions in Severe Asthmatic Lungs. Comput Math Methods Med 2018. [CrossRef]
[20] Miyawaki S, Tawhai MH, Hoffman EA, Lin C. Effect of Carrier Gas Properties on Aerosol Distribution in a CT-based Human Airway Numerical Model. Ann Biomed Eng 2012;40:1495−1507. [CrossRef]
[21] Freitag L, Ernst A, Unger M, Kovitz K, Marquette CH. A proposed classification system of central airway stenosis. Eur Respir J 2007;30:7−12. [CrossRef]
[22] Costanzo LS. Board Review Series, Physiology. Lippincott Williams & Wilkins; 2011.
[23] Sasko B, Thiem U, Christ M, Trappe H-J, Ritter O, Pagonas N. Size matters: An observational study investigating estimated height as a reference size for calculating tidal volumes if low tidal volume ventilation is required. PLoS ONE 2018;13:e0199917. [CrossRef]
[24] Zhao K, Scherer PW, Shoreh AH, Dalton P. Effect of Anatomy on Human Nasal Air Flow and Odorant Transport Patterns: Implications for Olfaction. Chem Senses 2004;29:365−379. [CrossRef]
[25] ANSYS. ANSYS fluent theory guide. ANSYS, Inc., Technology Drive Canonsburg, PA 15317. 2022.
[26] De Rochefort L, Vial L, Fodil R, Maitre X, Louis B, Isabey D, Caillibotte G, Thiriet M, Bittoun J, Durand E, Sbirlea-Apiou G. In vitro validation of computational fluid dynamic simulation in human proximal airways with hyperpolarized 3He magnetic resonance phase-contrast velocimetry. J Appl Physiol 2007;102:2012−2023. [CrossRef]
[27] Lin EL, Bock JM, Zdanski CJ, Kimbell JS, Garcia GJM. Relationship Between Degree of Obstruction and Airflow Limitation in Subglottic Stenosis. Laryngoscope 2018;1551−1557. [CrossRef]
[28] Ho CY, Liao HM, Tu CY, Huang CY, Shih CM, Chen JH, et al. Numerical analysis of airflow alteration in central airways following tracheobronchial stent placement. Exp Hematol Oncol 2012;1:23. [CrossRef]
[29] Qi S, Li Z, Yue Y, Han JW, Triest V, Kang Y, Qian W. Simulation analysis of deformation and stress of tracheal and main bronchial wall for subjects with left pulmonary artery sling. J Mech Med Biol 2015;2. [CrossRef]
[30] Zhu L, Gong X, Liu J, Li Y, Zhong Y, Shen J, et al. Computational Evaluation of Surgical Design for Multisegmental Complex Congenital Tracheal Stenosis. BioMed Res Int 2020. [CrossRef]
[31] Wilcox D. Turbulence Modeling for CFD volume 2. DCW Industries La Canada, CA. 1998.
[32] Mylavarapu G, Murugappan S, Mihaescu M, Kalra M, Khosla S, Gutmark E. Validation of CFD methodology used for human upper airway flow simulations. J Biomech 2009;42:1553−1559. [CrossRef]
[33] Qi S, Zhang B, Yue Y, Shen J, Teng Y, Qian W, et al. Airflow in Tracheobronchial Tree of Subjects with Tracheal Bronchus Simulated Using CT Image Based Models and CFD Method. J Med Syst 2018;42:6. [CrossRef]

[34] De Backer JW, Vos WG, Vinchurkar SC, Claes R. Validation of Computational Fluid Dynamics in CT-based Airway Models with SPEC/CT. Radiology 2010;257:854−862. [CrossRef]
[35] Qi S, Zhang B, Teng Y, Li J, Yue Y, Kang Y, Qian W. Transient Dynamics Simulation of Airflow in a CT-Scanned Human Airway Tree: More or Fewer Terminal Bronchi. Comput Math Methods Med 2017. [CrossRef]
[36] Yin Y, Choi J, Tawhai MH, Hoffman EA, Lin CL. Simulation of pulmonary air flow with a subject-specific boundary condition. J Biomech 2010;43:2159−2163. [CrossRef]
[37] Yin Y, Choi J, Hoffman EA, Tawhai MH, Lin CL. A multiscale MDCT image-based breathing lung model with time-varying regional ventilation. J Comput Phys 2013;24:168−192. [CrossRef]
[38] Lin CL, Tawhai MH, Hoffman EA. Characteristics of the Turbulent Laryngeal Jet and its effect on airflow in the human intrathoracic airways. Respir Physiol Neurobiol 2007;157:295−300. [CrossRef]
[39] Donzelli J, Brady S. The Effects of Breath-Holding on Vocal Fold Adduction. Arch Otolaryngol Head Neck Surg 2004;130:208−210. [CrossRef]
[40] Azarnoosh J, Sreenivas K, Arabshah A. Numerical simulation of tidal breathing through the human respiratory tract. J Biomech Eng 2020;142. [CrossRef]
[41] Xu X, Wu J, Weng W, Fu M. Investigation of inhalation and exhalation flow pattern in a realistic human upper airway model by PIV experiments and CFD simulations. Biomech Model Mechanobiol 2020;19:1679−1695. [CrossRef]
[42] Heenan AF, Matida E, Pollard A, Finlay WH. Experimental measurements and computational modeling of the flow field in an idealized human oropharynx. Exp Fluids 2003;35:70−84. [CrossRef]
[43] Lambert AR, O'Shaughnessy TP, Tawhai MH, Hoffman EA, Lin CC. Regional Deposition of Particles in an Image-Based Airway Model: Large-Eddy Simulation and Left-Right Lung Ventilation Asymmetry. Aerosol Sci Technol 2011;45:11−25. [CrossRef]